Chapter 8

The Super-Kamiokande and Other Detectors: A Case Study of Large Volume Cherenkov Neutrino Detectors

Shunichi Mine

Kamioka Observatory, ICRR, The Univ. of Tokyo, Higashi-Mozumi 456, Kamioka-cho, Hida-city Gifu 506-1205, Japan
mine@km.icrr.u-tokyo.ac.jp

8.1 Introduction

This chapter describes the Cherenkov neutrino detectors used in high-energy "high-E" (above about 0.1 GeV) physics experiments. These experiments include atmospheric neutrino oscillation measurements, nucleon decay searches (atmospheric neutrinos are the background), long baseline beam neutrino oscillation measurements, astrophysical neutrino searches, and so on. Each section also briefly mentions differences from low-energy "Low-E" ($\ll$100 MeV) physics measurements such as solar and supernova neutrinos.

We can only detect the presence of a neutrino if it interacts with the detector material. Neutrinos interact in two ways: charged-current (CC) interactions and neutral-current (NC) interactions. In CC interactions, the neutrino converts into the equivalent charged lepton (e.g., $\nu_e + n \to e^- + p$) and the experiments detect the charged lepton, as well as any other charged particles which emit Cherenkov light. In NC interactions, the neutrino remains a neutrino and we detect the other particles produced by the interaction.

 https://doi.org/10.1142/9789819801107_0008

In principle, CC interactions are easier to work with because electrons and muons have characteristic signatures in the Cherenkov detectors and are thus fairly easy to identify. Tau neutrinos are more difficult to identify for two reasons. Since the tau is more massive, the energy thresholds for the CC tau production (3.5 GeV) and the Cherenkov radiation of the tau lepton (2.7 GeV) are much higher. Also, the tau is extremely short-lived and therefore does not travel far enough to emit much Cherenkov light ($c\tau \sim 9 \times 10^{-5}$ m).

Since neutrinos only weakly interact with matter, neutrino detectors must be generally very large to detect a significant number of events. The combination of a transparent medium such as water with photomultiplier tubes (PMTs) as light sensors is beneficial for achieving a large effective volume at a low cost. Such a medium serves as a target for neutrino interactions and is well suited for propagating Cherenkov light from charged final-state particles and energetic photons. PMTs are chosen with wavelength sensitivity overlapping with the produced Cherenkov spectrum. A water purification system can remove radioactive substances and impurities and constantly circulate ultrapure water in the tank. The detectors are often built underground to isolate the detector from cosmic rays. In addition, detectors outside the main detector absorb or discriminate against incoming background particles from outside.

In order to extract as much information from each event as possible, the detector should have the following: good angular resolution so that the direction of the particle can be accurately reconstructed; good particle identification, allowing particle discrimination; good energy measurement so that the energy can be reconstructed; good time resolution so that the time evolution of transient signals can be studied; and so on.

In Section 8.2, the principle of the Cherenkov detector is explained using the Super-Kamiokande (Super-K or SK) detector [1–4]. SK is the world's largest water tank Cherenkov neutrino detector. This is the second-generation detector, with more mature experimental techniques than the first-generation IMB/Kamiokande detectors [5–7]. Since water Cherenkov detectors have a relatively sparsely instrumented readout per detector mass, using only PMTs to view a large active water volume, software for event reconstruction is very important. For this reason, the Appendix details how to reconstruct the events by software programs in SK. Section 8.3 summarizes past and present Cherenkov detectors. Section 8.4 presents the instrumentation and techniques of the hardware used in SK. Calibrating the detector is necessary and important for good physics results, so we explain this in Section 8.5. Some future prospects

with reference to next-generation experiments are discussed in Section 8.6. Finally, the achievements of Cherenkov neutrino detectors are summarized in Section 8.7.

8.2 Principle of Cherenkov Detectors

8.2.1 *Cherenkov radiation*

Water has a refractive index of 1.33 for visible light wavelengths, so light in water travels at 0.75c. Particles aren't affected by the refractive index, so a particle traveling at almost the speed of light through water will be traveling faster than the local speed of light in that medium. As an aircraft traveling faster than the speed of sound emits a sonic boom, similarly, a particle traveling through a transparent medium faster than the speed of light in that medium emits a kind of "light boom," a coherent cone of blue light known as Cherenkov radiation [8].

Figure 8.1 shows the geometry of Cherenkov radiation. The charged particle is traveling left to right at speed βc through a medium with

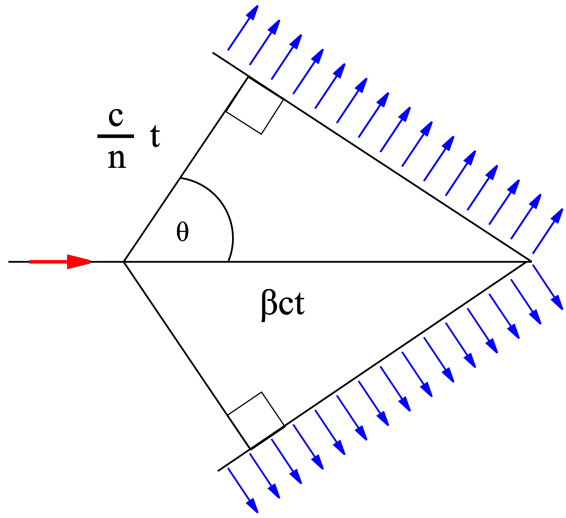

Figure 8.1. The geometry of Cherenkov radiation. From the left, a charged particle propagates, polarizing atoms and molecules around it. These atoms and molecules emit electromagnetic radiation, which propagates outward from each point along the track as a spherical wave. The wavefronts form a forward-propagating cone. The horizontal arrow is the velocity (v) of the charged particle, β is v/c, and n is the refractive index of the medium. The diagonal arrows show the direction of the radiation.

Source: Wikipedia.

refractive index n. The Cherenkov cone has half-angle θ given by

$$\cos\theta = \frac{1}{n\beta} \tag{8.1}$$

To emit Cherenkov light, β must be above $1/n$ ($\cos\theta$ must be less than 1). The energy threshold above which Cherenkov radiation is emitted is 0.8 MeV for an electron, 160 MeV for a muon, and 2.7 GeV for a tau. At the highest speeds ($\beta \sim 1$), the "Cherenkov opening angle" is about 41° in water and the Cherenkov light is radiated almost diagonally.

The spectrum of the Cherenkov light as a function of the wavelength λ is

$$\frac{dN}{d\lambda} = \frac{2\pi\alpha x}{c}\left(1 - \frac{1}{n^2\beta^2}\right)\frac{1}{\lambda^2}, \tag{8.2}$$

where $\alpha \approx 1/137$ (fine structure constant) and x is the length of the charged particle trajectory. A charged particle emits about 400 photons per centimeter pathlength in water in the wavelength region, 300−700 nm, where photomultiplier tubes (PMTs) are sensitive. Most visible Cherenkov radiation is in the violet range because of Eq. (8.2).

8.2.2 *Cherenkov light detection (overview)*

The detector water is contained in a tank lined with PMTs. For each event, the number of photons and time information for each PMT is recorded

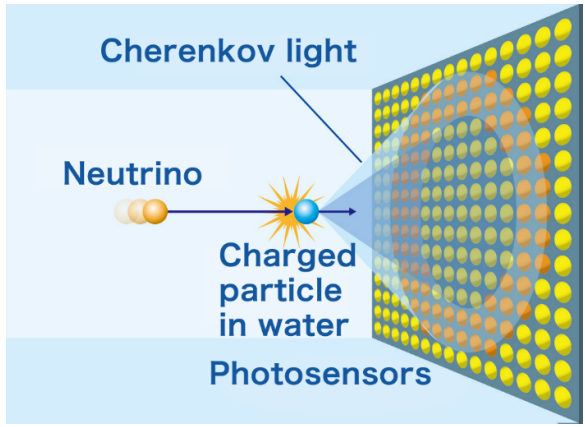

Figure 8.2. Cherenkov light is emitted in a cone shape along the direction of the charged particle. A tank wall is lined with photosensors (PMTs).

Source: Kamioka Observatory, ICRR, The University of Tokyo.

(Section 8.5.1.1). The Cherenkov light produced by a charged particle is reconstructed as a ring of hit PMTs (Fig. 8.2). Cherenkov light is emitted in a cone shape, surrounding the direction of the charged particle, and therefore the energy, direction, particle type, and so on are determined using information obtained from the PMTs, such as the amount of light detected and the ring shape (see Appendix). By assuming a type of neutrino interaction (e.g., quasi-elastic scattering), measurements of each charged particle in the final state can be used to reconstruct the original neutrino direction, energy, and so on.

Cherenkov light in the medium undergoes repeated wavelength-dependent absorption and scattering until it reaches the PMT. The attenuation of light due to absorption and scattering in water is measured as a function of wavelength (Sections 8.5.1.2 and 8.5.1.3) and is taken into account in the detector simulation and the event reconstruction for the physics analyses. For example, as discussed in Section 8.5.1.2, symmetric Rayleigh scattering is dominant at shorter wavelengths and absorption is dominant at longer wavelengths. The light transmittance is highest at around 400 nm. SK's PMT has the maximum quantum efficiency of the photocathode at about 400 nm [1]. The water transparency in SK is $\sim$100 m at around 400 nm, while in ice (Section 8.3.1.2) it is a couple of tens of meters.

Muons are leptons with a rest mass of 106 MeV/c^2 and a mean lifetime of 2.2×10^{-6} s. They have a relatively large mass with respect to that of the electron (0.511 MeV/c^2), and these particles do not participate in the strong interaction. Muons can penetrate longer distances in water ($\sim$0.5 cm/MeV) and are less susceptible to radiative energy losses compared to electrons. Over a broad energy range, the dominant energy loss mechanism is that of ionization. For example, the track length of a 1 GeV/c muon is about 5 m in water.

High-energy electrons and positrons primarily emit photons as they traverse the detector medium, a process called bremsstrahlung. Photons above a few MeV interact with matter primarily via pair production (an electron–positron pair). These processes (electromagnetic showers) continue, leading to a cascade of particles of decreasing energy until photons fall below the pair-production threshold, and electron (positron) energy losses become dominated by processes other than bremsstrahlung. Therefore, primary electrons have shorter track lengths than muons of the initial same energy.

As illustrated in Fig. 8.2, if a charged particle stops before reaching the surface of the water tank, it emits Cherenkov light at an angle determined by Eqs. (8.1) and (8.2) and is imaged on the tank surface as a Cherenkov

light ring. The size and thickness of the Cherenkov ring image on the tank surface are determined by the distance of the particle vertex to the surface, particle type, direction, and momentum of the charged particles. In contrast, if the charged particle penetrates the tank before stopping, it will result in a Cherenkov light pattern with no holes. See Section 8.4.11 for the classification of events according to where charged particles are created and stop.

Muons are basically single particles and make sharp rings, whereas electrons, positrons, and gamma ray photons initiate electromagnetic showers and the nearly parallel electrons and positrons in the shower combine to make a fuzzy ring, as shown in Fig. 8.3. Coulomb scattering of the electron also contributes to the fuzziness of the ring.

Neutrino interactions can produce mesons such as pions, as well as the charged lepton. In general, charged pions (a mass of $140\,\mathrm{MeV}/c^2$ and a lifetime of $2.6 \times 10^{-8}\,\mathrm{s}$) are difficult to distinguish from muons, but they may be able to be identified by using the properties of hadronic scattering (A.1.8).

When multiple Cherenkov rings are observed, the direction, particle type, and momentum are obtained for each ring, as in the case of the single-ring event. A neutral pion π^0 (a mass of $135\,\mathrm{MeV}/c^2$ and a lifetime of $8.4 \times 10^{-17}\,\mathrm{s}$) immediately decays into two gammas and is detected as two "electron-like" rings. Figure 8.4 shows a typical reconstructed invariant mass distribution of the neutral pion events. See Section A.1 for details of reconstructing the event in the high-E physics analyses.

Tau leptons (a mass of $1.78\,\mathrm{GeV}/c^2$ and a lifetime of $2.9 \times 10^{-13}\,\mathrm{s}$) produced in CC ν_τ interactions decay quickly to secondary particles. Due to the short lifetime of the tau lepton, it is impossible to directly detect taus in SK. The decay modes of the tau lepton are classified into leptonic and hadronic decay, based on the secondary particles in the decay. The leptonic decays produce neutrinos and an electron or a muon. These events look quite similar to the atmospheric CC ν_e or ν_μ background. The hadronic decays of the tau are dominant and produce one or more pions, plus a neutrino. The existence of extra pions in the hadronic decays of tau allows for the separation of the CC ν_τ signal from CC ν_μ, CC ν_e, and NC background. Multiple-ring events are relatively easy to separate from single-ring atmospheric neutrino events. However, the multi-ring background events, resulting from multi-pion/DIS atmospheric neutrino interactions, are difficult to distinguish from the tau signal. Simple selection criteria based on kinematic variables do not efficiently identify CC ν_τ events.

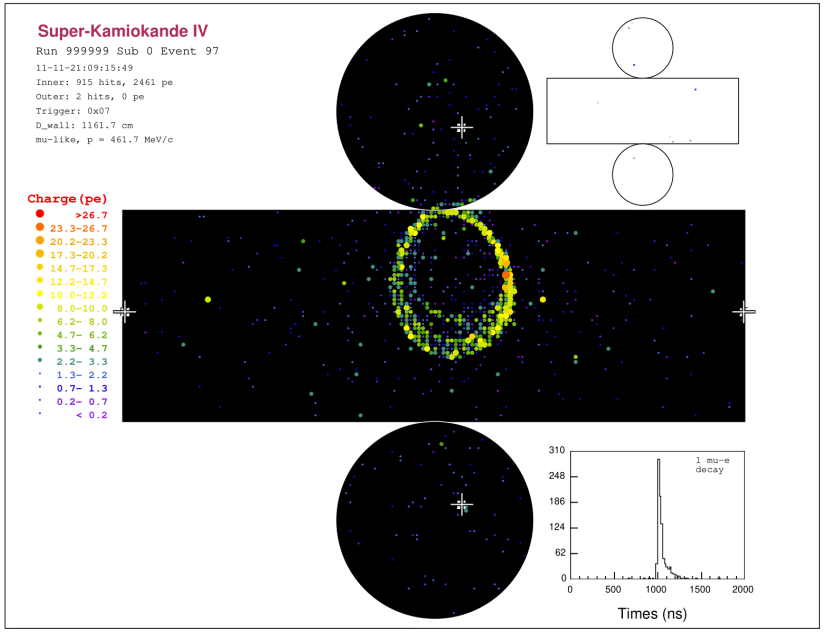

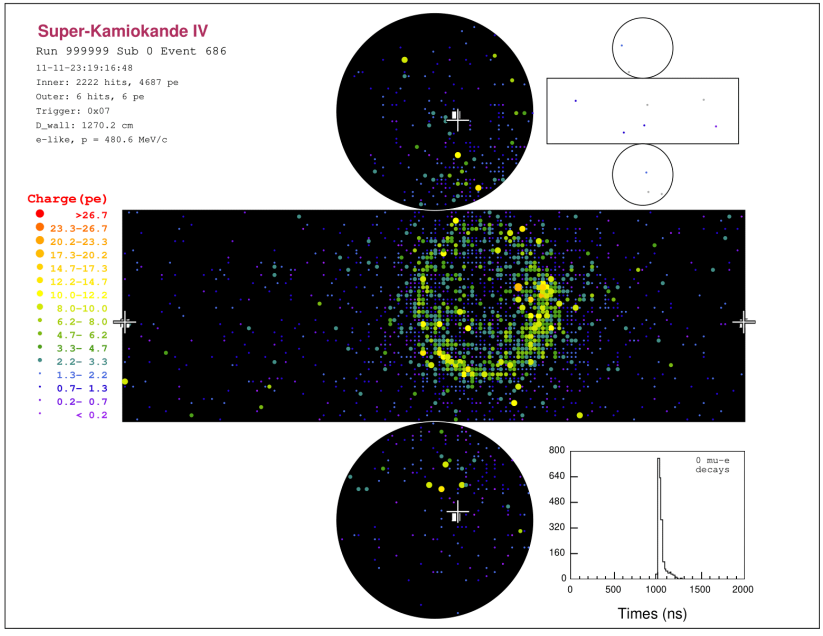

←

Figure 8.3 (***Continued***). The upper and lower displays are a typical muon and an electron-simulated event, respectively, in SK. In this example, a muon (electron) of about 500 MeV/c was created near the center of the tank, which headed toward the barrel wall. The display shows the expansion of the vertical cylindrical detector (∼40 m diameter and ∼40 m height). The larger and smaller figures are the inner detector (ID) and the outer detector (OD), respectively. See Section 8.4 for each detector component. The color dots visualize which PMTs were hit in the event. The color correspond to the number of photoelectrons registered at that particular PMT. The timing distribution of the hit PMTs is shown at the bottom right.

Source: Kamioka Observatory, ICRR, The University of Tokyo.

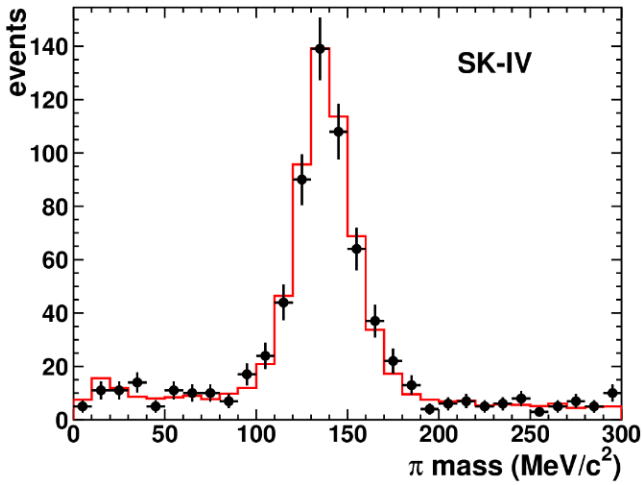

Figure 8.4. Reconstructed invariant mass distribution of the atmospheric-neutrino-induced π^0 events in the observed data (dot) and simulated atmospheric neutrino samples (histogram) in SK [9]. Two "electron-like" ring events are selected without any tagged "Michel electron" (an electron from a muon decay) in the fiducial volume (defined as a distance from the reconstructed vertex to the nearest inner detector wall is greater than 2 m). See Section A.1 for the meaning of each cut parameter.

In order to statistically identify events with the expected characteristics that differentiate signal and background, a multivariate method is applied in the SK analysis, based on the reconstructed parameters [10].

The final-state charged particles used in lower-energy "low-E" ($\ll$100 MeV) neutrino data analysis are almost exclusively electrons or gamma rays. For example, for electrons at SK, approximately several photoelectrons per MeV (pe/MeV) are detected at the PMT. Since more than 10,000 PMTs (Section 8.4.3) are mounted on the inner detector

(ID) wall of SK, the number of photoelectrons per PMT for each low-E neutrino event is typically one. Therefore, unlike for high-E events, low-E event reconstruction basically does not use PMT charge information but only PMT hit and time information. The high-E and low-E event reconstructions, respectively, are detailed in Appendix A. In high-E physics data analyses, we use events above the energy threshold of several tens of MeV, so a few MeV radioactivity is not a background.

8.3 Past and Present Cherenkov Detectors

8.3.1 *Water Cherenkov experiments*

8.3.1.1 *Densely instrumented artificial tanks*

The pioneering Irvine–Michigan–Brookhaven [5, 7] (IMB, 1982–1991) and Kamioka Nucleon Decay Experiment [6] (Kamiokande, 1983–1996) experiments, made famous by their observations of SN 1987A, were originally conceived as detectors for nucleon decay. Atmospheric neutrinos are a background for the nucleon decay search as the neutrino interactions produce charged particles, sometimes kinetically indistinguishable from the nucleon decay signal.

Super-Kamiokande [1–4] (1996−present) was designed to extend and improve upon the experience gained by its scientific predecessors, the Kamiokande and IMB experiments, as well as to detect high-E neutrinos, search for nucleon decay, study solar and atmospheric neutrinos, and watch for supernovae in the Milky Way galaxy. As an example, the results of the discovery of atmospheric neutrino oscillations published in 1998 [11] are shown in Fig. 8.5. SK has also been used as a far detector for long-baseline beam neutrino oscillation experiments: K2K [12] (1999–2004) and T2K [13] (2010−present).

The K2K experiment used a 1-kiloton (1 KT) water Cherenkov neutrino detector located at about 300 m from an aluminum neutrino production target to determine the neutrino beam characteristics and to measure neutrino cross-sections [12,14,15]. This 1KT "near detector" was a scaled-down version of the 50-kiloton SK "far detector." The vertical cylindrical tank ($\sim$11 m in diameter and $\sim$11 m in height), the PMT type, the photocoverage (40%), the water purification system, the readout electronics, the event reconstruction algorithms, and the detector calibration methods were basically the same as those in SK. Having the same detector technology along the beam line allowed for a significant reduction of

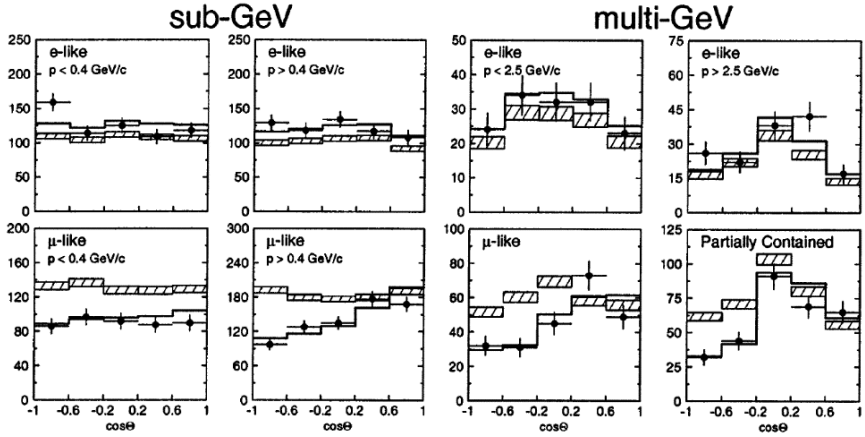

Figure 8.5. Zenith angle distributions of muon-like and electron-like events for sub-GeV and multi-GeV datasets [11]. Upward-going particles (longer atmospheric neutrino travel length) have $\cos\Theta < 0$ and downward-going particles (shorter travel length) have $\cos\Theta > 0$. The hatched histogram shows the Monte Carlo expectation. The bold line is the best-fit expectation for $\nu_\mu \leftrightarrow \nu_\tau$ oscillations. "Partially Contained" is explained in Section 8.4.11.

detector uncertainties related to the prediction of the neutrino interaction rate and energy spectrum in SK before the neutrino oscillations. The detector performance, including the energy reconstruction and particle identification, was similar to that achieved in high-E analyses at SK. The 1KT detector also provided high statistics measurements of neutrino–water interactions.

8.3.1.2 *Sparsely instrumented natural water (neutrino telescopes)*

A very large volume of natural water can be instrumented with a sparse array of PMTs dispersed throughout the volume [16–20]. The cone geometry is not visually apparent but can be reconstructed using the time at which each hit PMT records its pulse, where the Cherenkov opening angle is known because these detectors observe only high-E particles. The threshold of these detectors depends on the spacing of the PMTs and is typically high (tens or hundreds of GeV). These detectors typically reconstruct muons, which make a long straight track, much better than electrons, which deposit all their energy in a fairly small volume and are thus seen by fewer PMTs.

The pioneering project for the construction of an underwater neutrino telescope was developed by the DUMAND collaboration [16], which attempted to deploy a detector off the coast of Hawaii in the 1980s. In parallel, the BAIKAL collaboration [17] began to build a similar detector system in the Baikal Lake. These experiments have been continued in the Mediterranean Sea by the ANTARES collaboration [18], which completed in 2008 the construction of the largest neutrino telescope ($\sim$0.1 km^2) in the northern hemisphere.

Regarding deep ice, a major step toward the construction of a large neutrino detector was made by the AMANDA collaboration [19], which completed their detector in 2000, and then IceCube, completed in 2011, with a total of 86 scheduled strings [20].

The detection principle to search for high-E neutrinos of astrophysical origin relies mainly on the detection of Cherenkov light emitted from an up-going muon induced by a ν_μ that penetrated the Earth. The detection strategy is based on the measurement of the intensity and arrival time of Cherenkov light produced along the muon track on a three-dimensional array of PMTs. A typical event display which shows an upgoing muon event is shown in Fig. 8.6.

The main problem in track reconstruction is that, at the energy of interest in neutrino telescopes (namely, from about 100 GeV to about 1 PeV), high-energy muons can produce electromagnetic radiation in the interaction with the Coulomb field of the nuclei in the material. These radiative energy loss processes generate secondary charged particles along the muon trajectory, which also produce Cherenkov radiation that arrives after the ideal Cherenkov cone. These track-correlated processes are stochastic, and their relative photon yield fluctuates with distribution around the true track position, depending on the physics of the underlying secondary process and on the properties of the detector. In addition, the arrival time of the photons on the PMTs has poor resolution because of the optical properties of the material in which the tracks propagate. The dominant effect is the scattering that depends strongly on the distance of the PMT from the track. Moreover, environmental background contributes to a large noise counting rate. In an undersea neutrino detector, the decay of radioactive elements in the water, mainly the β-decay of potassium isotope ^{40}K, generates electrons that produce Cherenkov light, resulting in an isotropic background of photons. These photons may degrade the hit pattern of a neutrino-induced event and consequently the event reconstruction, even when coincidence methods significantly reduce the contamination.

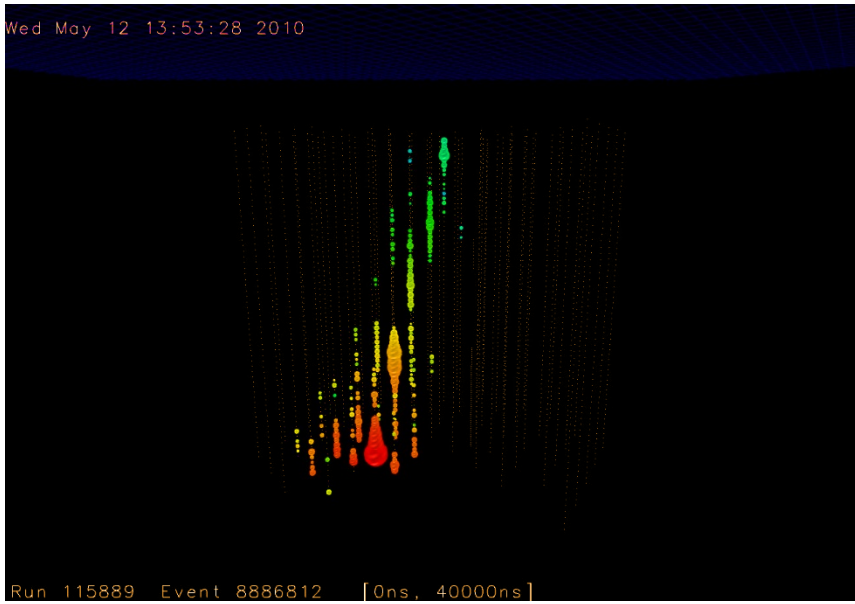

Figure 8.6. An upgoing muon event from the 59-string configuration. The light collected by each sensor is shown with a gray sphere. The color shows the time sequence. The size reflects the number of photons detected.

Source: IceCube Collaboration.

8.3.2 *Other Cherenkov experiments*

The Sudbury Neutrino Observatory [21] (SNO, 1999–2006) used 1,000 tons of ultrapure heavy water contained in a 12 m diameter vessel made of 5 cm thick acrylic plastic. This target was observed by 9,456 PMTs on a 17.8 m diameter support structure contained within a cylindrical cavern that was 22 m in diameter and 34 m height and filled with ordinary ultrapure water. The experiment was located 2 km underground in an active nickel mine near Sudbury, Ontario. Heavy water, D_2O, replaces normal hydrogen with its heavier isotope deuterium (^{2}H or D), whose nucleus contains a neutron in addition to the proton of normal hydrogen. Deuterium is extremely weakly bound and therefore easily broken up when struck. Therefore, in addition to the neutrino interactions visible in a regular water detector, a neutrino can break up the deuterium in heavy water in two different ways: CC reactions result in an electron signal and are sensitive to only electron neutrinos, while NC reactions can break apart a deuteron, resulting in a neutron signal and are sensitive to all active neutrino flavors.

SNO used three different techniques to detect neutrons, all viable due to the presence of heavy water. The first of these techniques [22] used pure D_2O in which neutron capture on D resulted in a 6.25 MeV gamma ray. With the addition of 2 tons of NaCl to the D_2O [23], neutrons captured by ^{35}Cl with a higher capture cross-section resulted in a gamma cascade of 8.6 MeV and higher neutron detection efficiency. These events can be statistically separated from the electron signal making use of parameters sensitive to the event isotropy. In the final phase of the experiment, the salt was removed and ^{3}He proportional counters were deployed [24] to measure the neutron signal independently of the Cherenkov signal.

8.4 Detector Components in SK

We introduce the instrumentation and techniques of the hardware used in SK [1–4].

8.4.1 *Detector location*

SK is located in the Mozumi mine of the Kamioka Mining and Smelting Company, Gifu, Japan. The detector cavity lies under the peak of Mt. Ikenoyama, with 1,000 m of rock, or 2,700 m-water-equivalent (m.w.e.) mean overburden (Fig. 8.7).

Cosmic ray muons with energy of less than 1.3 TeV cannot penetrate to a depth of 2,700 m.w.e. The observed muon flux, which does not pose a significant background for the experiment, is $6 \times 10^{-8}\,\mathrm{cm}^{-2}\,\mathrm{s}^{-1}\,\mathrm{sr}^{-1}$.

8.4.2 *Water tank*

The SK detector consists of a welded stainless-steel vertical cylindrical tank, 39 m in diameter and 42 m in height, with a total nominal water capacity of 50,000 tons. The tank top itself is used as a platform to support electronics huts, equipment for calibration, water quality monitoring, and other facilities.

On the top of the tank, there are multiple feedthroughs with an inner diameter of $\sim$20 cm at intervals of several meters along the x and y axes (z is defined vertically upward) and along the outer wall for detector calibration (Section 8.5) of the inner detector (ID) and the outer detector (OD), respectively. For calibrations relevant to low-E physics (solar neutrinos, supernova neutrinos, and so on), an electron linear accelerator "LINAC" [25] is installed at the top of the tank toward the $+x$ direction.

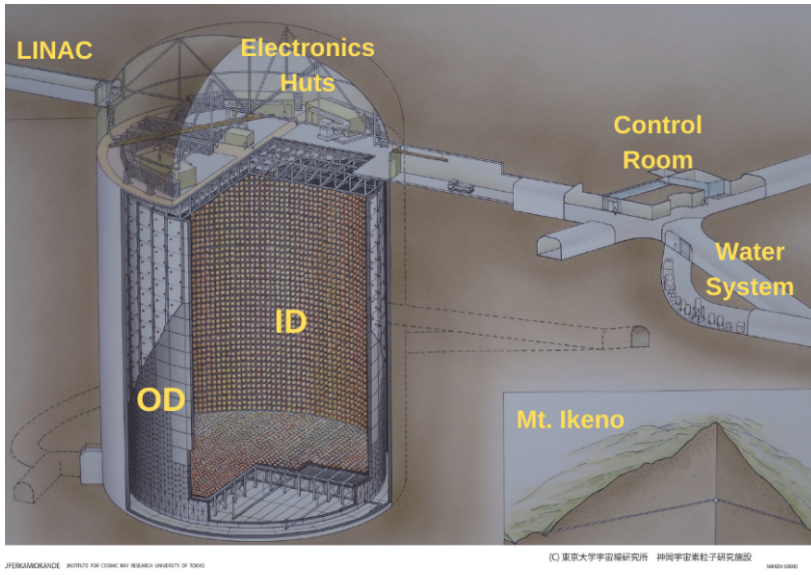

Figure 8.7. A sketch of the SK detector site, under Mt. Ikenoyama.
Source: Kamioka Observatory, ICRR, The University of Tokyo.

The electron beam is bent 90° toward the $-z$ direction and delivered into the tank through the ID calibration holes.

8.4.3 *ID PMTs*

Within the tank, a stainless-steel framework of thickness 55 cm, spaced approximately 2–2.5 m inside the tank walls on all sides, supports separate arrays of inward-facing and outward-facing PMTs. The inward-facing array consists of 11,146 Hamamatsu Type R3600 50 cm diameter hemispherical PMTs in SK-I (1996–2001). These PMTs have a photocathode made of bialkali (Sb-K-Cs), with a maximal photon conversion probability in the wavelength range of Cherenkov light (Eq. (8.2)). The inward-facing PMTs, and the volume of water they view, are referred to as the inner detector (ID).

The experiment began data-taking in 1996 and was shut down for maintenance in 2001. This initial phase is called SK-I. Due to an accident during the ensuing upgrade work, the experiment resumed in 2002 with only about half of its original number of ID-PMTs (SK-II). To prevent similar accidents, all ID-PMTs were encased in fiber-reinforced plastic (FRP) cases with ultraviolet transparent acrylic front windows starting from SK-II. Such protective covers are needed to avoid any cascade implosion of the PMTs.

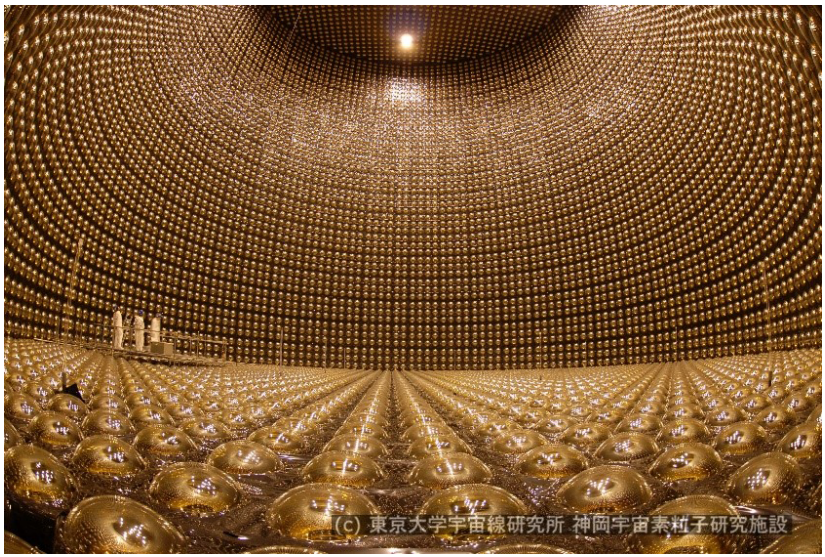

Figure 8.8. The inner detector during the full reconstruction in 2006. The light-colored figures in the lower left are three people.

Source: Kamioka Observatory, ICRR, The University of Tokyo.

Figure 8.8 shows the ID during the full reconstruction before filling water toward SK-III (2006–2008) in 2006.

The density of PMTs in the ID was such that effectively about 40% (20%) of the ID surface area was covered by a photocathode in SK-I, SK III-VIII (SK-II). Although the photo coverage was half that of other eras, SK-II (2002–2005) has obtained a detector performance that is almost the same as other detector phases in high-energy physics analyses. See Refs. [26, 27], for example.

8.4.4 *OD PMTs*

Optically isolated from the ID is an array of 1,885 outward-facing Hamamatsu R1408 20 cm diameter hemispherical PMTs in SK-I. These PMTs, and the water volume they view, are referred to as the outer detector (OD). The optical isolation of ID and OD is made by black polyethylene terephthalate sheets ("black sheets") on the inside of the barrier and highly reflective Tyvek® sheets on its outside. Tank walls are also lined with Tyvek® sheets. Each OD PMT is attached to a 50 cm × 50 cm acrylic wavelength shifting (WS) plate. These features improve light collection efficiency for the OD, compensating for the relatively sparse PMT array.

8.4.5 *Compensation coils*

Twenty-six sets of horizontal and vertical coils are arranged around the inner surface of the tank to neutralize the geomagnetic field that would otherwise affect photoelectron trajectories in the PMTs. Before and during filling of the tank with water for SK-III, and with the coils carrying their design currents, the residual fields at 458 PMT locations around the detector were measured using a device that can simultaneously measure the magnetic field vector along three orthogonal axes.

During the SK refurbishment tank open work between SK-IV (2008–2018) and SK-V (2019–2020), we remeasured the residual magnetic field for all the PMTs with a tilted-corrected and waterproof 3-axis magnetometer, providing a magnetic field map of the whole tank. These results confirm that the geomagnetic field is successfully reduced by the coils. Dynode directions are also recorded for all the PMTs.

The geomagnetic compensation coil cables failed in three places at the end of 2023. In 2024, SK-VIII (2024 - present) was started after we successfully installed new coils to restore geomagnetic field cancellation.

8.4.6 *PMT HVs and electronics*

The cables from each PMT for both ID and OD are brought up to the top of the tank and connected to the signal digitizers and the HV supplies in four quadrant electronics huts. The PMT cables have the same length to maintain the delay, and the signal qualities are the same. The ID (OD) PMTs are operated with a gain of about 10^7 at a supply HV ranging from 1,600 to 2,000 V (1,300–1,800 V). See Section 8.5.1.1 for the PMT HV determinations.

At the start of the SK-IV period in 2008, the front-end electronics were upgraded to a system with an ASIC based on a high-speed charge-to-time converter (QTC), the QBEE (QTC-based electronics with Ethernet) [28] module for both ID and OD. This allows us to record all hits above the discriminator threshold, including the dark noise hits. All the hit data are sent to the front-end readout computers without filtering, and the events are defined using the software trigger. Each ID PMT has a dynamic range from 1 photoelectron (pe) to about 300 (1,000) pe in SK-I-III (from SK-IV).

An electronics hut, the "Central Hut," contains electronics and associated computers for GPS time stamping. Also, various detector monitoring systems are located there.

8.4.7 *Online software trigger system*

The Cherenkov photon signal for a given event is emitted promptly along particle tracks and clusters within a few hundred ns, but dark noise is random and does not form a timing cluster. Pulses on PMTs exceeding a charge threshold corresponding to roughly 0.25 pe are registered as hits, all of which are processed by a software trigger system. The number of hits ($\sim$6 hits/MeV except SK-II) within 200 ns is counted, and if the number of hits exceeds a certain value (equivalent to a few MeV), a trigger is applied. The online trigger efficiency for the high-E ($>\sim$100 MeV) physics events is 100%.

T2K-SK beam events (Section 8.3.1.1) are selected by requiring the time of the event in SK to coincide with the expected time of arrival of the neutrino beam. For T2K analyses [13], all hits occurring in the 1 ms windows centered on each beam spill arrival are written to disk. Beam spills are excluded from the analysis if they coincide with problems in the data acquisition system or the GPS system used to synchronize SK with the accelerator at J-PARC. Additionally, spills that occur within 100 μs of a beam-unrelated event are rejected to reduce the contamination of T2K data with cosmic-ray muon Michel electrons.

8.4.8 *GPS system*

The K2K experiment (Section 8.3.1.1) required synchronization of clocks with $\sim$100 ns accuracy at the near and far detector sites (KEK and SK, respectively), which are separated by 250 km [29]. GPS provides a means for satisfying this requirement at a very low cost. Commercial GPS receivers output a 1 pulse per sec (1 PPS) signal whose leading edge is synchronized with GPS seconds rollovers to well within the required accuracy. For each beam spill trigger at KEK, and each event trigger at SK, 50 MHz free-running Local Time Clock (LTC) modules at each site provide fractional second data with 20 ns ticks. At each site, two GPS clocks run in parallel, providing hardware backup as well as data quality checks.

Basically, the same GPS system is used for the T2K experiment with some updates. The standard GPS receivers installed in Kamioka and Tokai (the near detector site) cannot verify whether their outputs are well synchronized with each other. To overcome this problem, special GPS receivers, capable of providing information for the "Common View" method, were installed at both sites. The Common View method uses information from the same GPS satellites, which are visible from different

locations simultaneously, and provides the data to compare timing signals from standard GPS receivers. These devices confirm that the reference clock signals from two GPS receivers in Kamioka and Tokai are synchronized and stable within the order of $\mathcal{O}(100\,\text{ns})$.

8.4.9 *Water purification system*

The water used in SK is sourced from natural water in the Kamioka mine. To maximize water transparency and minimize backgrounds due to natural radioactivity, the water used to fill the SK tank is highly purified by a multi-step system including deionization (DI) resins, filtration, reverse osmosis (RO), and degasification. Water purity is maintained by recirculation through the purification system.

The water circulation pattern in the detector can be manipulated by changing the temperature of the water that is fed into the bottom of the detector from the recirculation system. Since the temperature difference between the top of the tank and the bottom of the tank is only about 0.1° C, the water temperature should be controlled with better than 0.01° precision. To achieve temperature control, a thermometer with 0.0001° precision is a component of the recirculation system and its output is fed back to the water-cooling system. The same thermometers are placed at eight positions in both the ID and the OD to monitor the water temperature and their time dependence.

In order to improve SK's neutron detection efficiency and to thereby increase its sensitivity to the diffuse supernova neutrino background flux, 13 tons of $Gd_2(SO_4)_3{\cdot}8H_2O$ (gadolinium sulfate octahydrate) was dissolved into the SK tank in 2020, marking the start of the SK-Gd phase of operations, SK-VI [3] (2020−2022). In 2022, an additional 26 tons of $Gd_2(SO_4)_3{\cdot}8H_2O$ was dissolved, and SK-VII [4] (2022–2024) was started yielding a 75% neutron capture efficiency on Gd. In the recirculation system for the gadolinium sulfate water, DI and RO are omitted, and instead, special anion and cation resins that keep Gd^{3+} and SO_4^{2-} are deployed. Nevertheless, the attenuation length of the Cherenkov light in the SK tank (Section 8.5.1.3) is sufficiently long and stable for physics analyses.

8.4.10 *Fresh air system*

To mitigate the relatively high radon background present in the air of the mine, the tank area is supplied with fresh air pumped in from a site outside and well away from the mine entrance. The flow rate and temperature

of the air sent from a prefabricated hut ("Radon Hut") outside the mine entrance to the SK are a few 100 m^3/min and about 10° C, respectively. It is necessary to lower the temperature in order to reduce the condensation in the pipe that sends air into the mine. Air is cooled with source water in the mine and a chiller. Radon concentration is checked by monitors installed in the Radon Hut and at several locations in the SK.

This Rn-reduced air is supplied to the gap between the water surface and the top of the SK tank and is kept at a slight overpressure to help prevent ambient radon-laden air from entering the detector. The air purification system consists of three compressors, a buffer tank, dryers, filters, and activated charcoal filters. The SK Rn-reduced air system uses 50 L of chilled activated charcoal to remove Rn from throughput air. Since it is known that the Rn-trapping efficiency of activated charcoal increases significantly below temperatures around −60° C, the system was upgraded in 2013 to bring its cooling power down from −40° C in the previous design to below this threshold. In order to do so, the system's coolant was changed to 3 MNOVEC^{TM} 7100 and its refrigerator upgraded [30]

8.4.11 *Event classifications*

Neutrino interactions are detected via the Cherenkov light emitted by the charged particles produced (Section 8.2). Events due to entering charged particles can be identified using the OD PMTs. Neutrino interaction candidates produced in the ID are defined as events producing Cherenkov light in the ID, with no evidence of entering particles in the OD. Neutrino events produced in the ID are termed "fully contained" if there is no activity in the OD indicating exiting or entering particles.

Events originating in the ID with OD light patterns consistent with exiting particles are termed "partially contained." For these events, the energy deposited in the detector is only a lower limit on the neutrino energy. Upward-going muons, which are assumed to be products of neutrino interactions in the rock below SK, are also recorded. For upward muons, Cherenkov light patterns consistent with an entering muon are required.

Finally, downward-going muons (cosmic-ray muons), products of meson decay in the atmosphere, are observed at a net rate of about 2 Hz. These events provide useful housekeeping and calibration data. For example, through-going muons are used to monitor the attenuation length of Cherenkov light in water, and stopping muons are used to check the energy scale for physics analyses (Section 8.5.1.3).

8.5 Detector Calibrations

We describe the calibration methods in SK-IV [2], in which new readout QBEE electronics (Section 8.4.6) have been operating.

8.5.1 *ID calibration*

8.5.1.1 *PMT and electronics calibrations*

For the PMT charge calibration, it is necessary to measure the "gain" and "QE" of each PMT. "Gain" is a conversion factor from the number of photoelectrons to charge (pC), and "QE" is defined as the product of the quantum efficiency and the photoelectron collection efficiency on the first dynode of the PMT.

An appropriate HV value for each PMT was determined so that all PMTs output approximately the same charge. A scintillator ball connected to an Xe lamp was placed in the center of the SK tank to emit isotropic light. The number of photons reaching each PMT is affected not only by the difference in geometrical distance within the large cylinder tank (Section 8.4.2) but also by the position dependence of light propagation due to water quality and light reflection on the tank surface (Section 8.5.1.2). To avoid this problem, 420 "standard PMTs" with HV pre-determined using a pre-calibration system were installed in the tank. PMTs at the same distance from the light source are grouped and the standard PMT placed in each group is used as a reference. The scintillator ball connected to the Xe lamp remains in the center of the tank as a monitor of PMT gain as well as other measurements.

The PMT gain measurement is performed in two stages. First, the relative gain is measured and then the absolute gain is calibrated. A diffuser ball connected to a nitrogen-laser-driven dye laser through an optical fiber was placed in the tank for the relative gain measurements. High light intensity (sufficient number of photons reaching each PMT) and low light intensity ($\sim$1 photon reaching each PMT) measurements were made. The former measures the charge $Q_{\rm obs}(i)$ and the latter measures the number of hits $N_{\rm obs}(i)$ in each PMT i:

$$Q_{\rm obs}(i) \propto I_s \times a(i) \times \varepsilon_{\rm qe}(i) \times G(i) \tag{8.3}$$

$$N_{\rm obs}(i) \propto I_w \times a(i) \times \varepsilon_{\rm qe}(i) \tag{8.4}$$

where I_s and I_w are the average intensities of the high- and low-intensity flashes, respectively, $a(i)$ is the acceptance of PMT, $\varepsilon_{\rm qe}(i)$ denotes its QE,

and $G(i)$ is its gain. The gain of each PMT can be derived by taking the ratio of Eqs. (8.3) and (8.4), except for a factor common to all PMTs:

$$G(i) \propto \frac{Q_{\text{obs}}(i)}{N_{\text{obs}}(i)} \tag{8.5}$$

Then the relative gain of each PMT is derived by normalization with the average gain over all PMTs. These relative gains are used as corrections in the conversion of each PMT's output charge to an observed number of photoelectrons.

The absolute gain is calibrated from the cumulative single-photoelectron charge distribution for all PMTs. A Ni-Cf ("nickel source") deployed in the center of the tank is used for this purpose. It produces isotropic gamma rays of about 9 MeV when thermal neutrons from the spontaneous fission of the californium capture on the nickel. To evaluate the distribution below the usual threshold of 0.25 pe, data with double the usual PMT gain and half the usual discrimination threshold were taken (Fig. 8.9). The value averaged over the whole pC region was defined as the conversion factor from pC to single photoelectron. The single-photoelectron charge distribution is implemented in the SK detector simulation ("SK-MC").

The nickel source data are also used to measure the relative QE. As shown in Eq. (8.4), the number of hits observed at each PMT is proportional to each QE value when a source with sufficiently low light intensity is used. The nickel source data were taken after achieving uniform water quality by causing water convection in the tank. The uniform water quality can be identified by measuring the water temperature profile in the tank (Section 8.4.9). The ratio of the number of hits between data and MC is implemented in the SK-MC as the relative QE for each PMT.

The charge linearity of the whole system combined with PMT and readout electronics was measured using the laser system. It is necessary to cover all possible charge ranges including the saturation region (above a few 100 pe). For this purpose, data were taken with the diffuser ball placed at an off-center location in the tank. The average nonlinearity measured for all PMTs is taken into account in the SK-MC.

The time response of each readout channel, including PMTs and readout electronics, must be calibrated for precise reconstruction of the event (Appendix A). The response time of readout channels can vary due to differences in the transit time of PMTs, lengths of PMT signal cables, and processing time of readout electronics. In addition, the timing of discriminator output depends on the pulse heights of PMTs since the rise

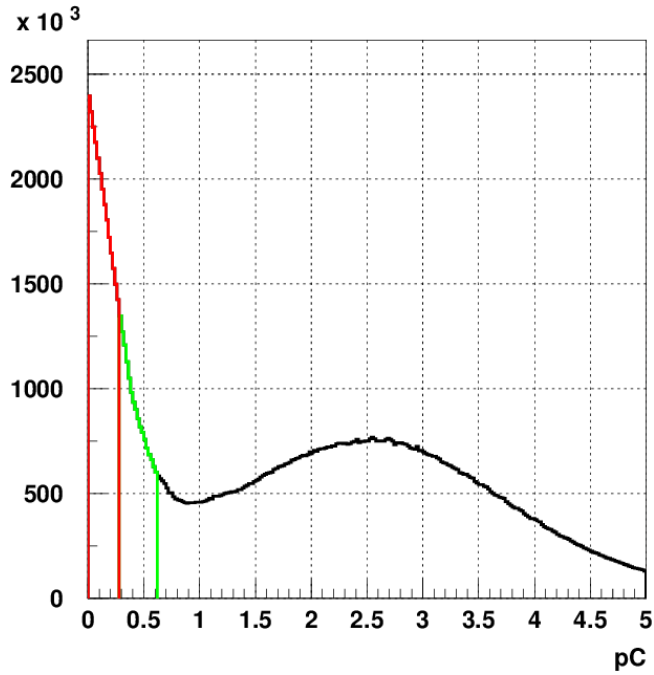

Figure 8.9. The single-photoelectron charge distributions in pC unit for nickel source data [2]. The black line ($>\sim$ 0.6 pC) shows the data with normal PMT gain, the green line ($\sim$0.3–0.6 pC) shows the data with double gain and half threshold, and the red line below $\sim$0.3 pC is linear extrapolation.

time of a large pulse is shorter than that of a smaller one. This is known as the "time-walk" effect.

The overall processing time and the time-walk effect were measured by injecting fast light pulses from a gas flow nitrogen laser into PMTs in the tank. The wavelength of the laser light is shifted to 398 nm by a dye, where the convoluted response with Cherenkov spectrum (Eq. (8.2)), light absorption spectrum (Fig. 8.11), and quantum efficiency of the PMTs is almost maximum. The fast light is guided into the tank by an optical fiber and injected into a diffuser ball located near the center of the tank to produce an isotropic light. Figure 8.10 shows a typical scatter plot of the time-charge "TQ" distribution for one readout channel. The calibration constants, called the "TQ-map," are derived by fitting the TQ distribution to polynomial functions. Each readout channel has its own TQ-map used to correct the time response.

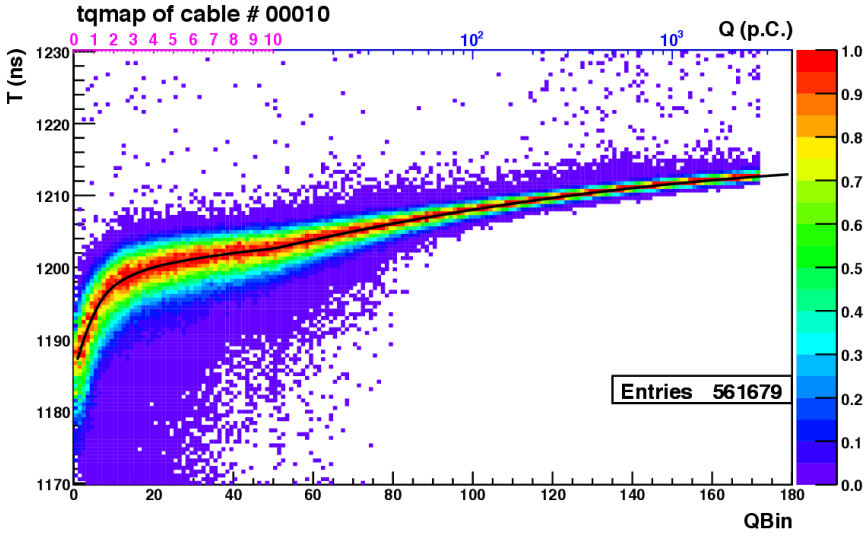

Figure 8.10. Typical TQ distribution for a readout channel [2]. The horizontal axis is the charge (QBin) of each hit, and the vertical axis is the time-of-flight-corrected timing (T) of the hits. Larger (smaller) T corresponds to earlier (later) hits in this figure.

The timing resolution is evaluated using the same dataset used for the TQ-map evaluation. All PMT timing distributions corrected by their TQ-maps are fitted by an asymmetric Gaussian to evaluate the timing resolution in each charge region. The results are implemented in the SK-MC.

For the real-time monitoring of the time response, SK employs a nitrogen laser that uses sealed nitrogen as a gain medium and is better suited for continuous operation. The light output of the dye system is injected into the same diffuser ball used for the TQ-map measurement.

8.5.1.2 *Calibration for photon tracking*

By injecting a collimated laser beam into the SK tank and comparing the timing and spatial distributions of the light with MC, we can extract light absorption and scattering coefficients as functions of wavelength. The earlier timing PMT hits come from scattered photons, while the later timing hits represent photons reflected by the PMTs and black sheets. The total number of scattered photons and the shape of the time distribution are used to tune the symmetric and asymmetric scattering and the absorption parameters for the SK-MC in each SK phase. Figure 8.11 shows each water

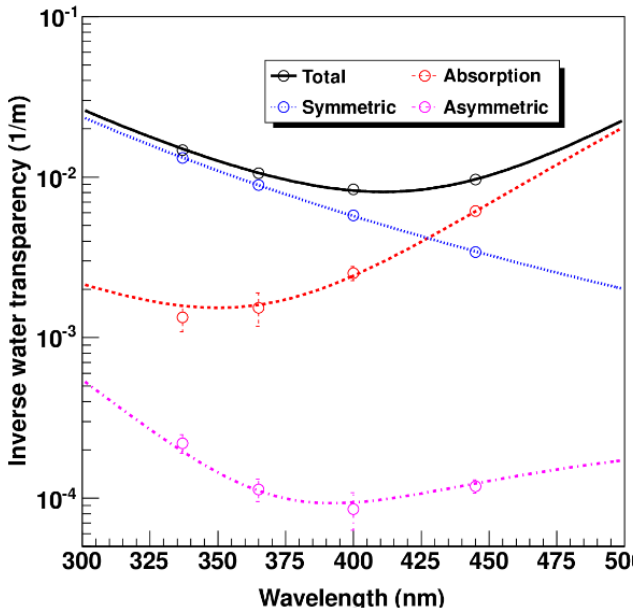

Figure 8.11. Typical water quality parameters implemented in the SK-MC [2]. The points are the data obtained in April 2009. Each line through the points for absorption (dashed), symmetric scattering (dotted), and asymmetric scattering (dash-dotted) shows the fitted functions while the top line shows the total of all fitted functions added together.

quality parameter as a function of wavelength. Time variation of each parameter is monitored at several wavelengths using several light injectors directed vertically and horizontally in the tank.

It has been found that water quality depends on position in the tank, especially vertically, and mainly comes from differences in absorption. This is because the pure water enters from the bottom area of the OD in the tank (Section 8.4.9). The vertical dependence of absorption in the SK-MC is determined from the monthly nickel source data and monitored with the real-time Xe system (Section 8.5.1.1).

Light reflection at the PMT surface in the SK-MC is tuned using the same laser data used to determine the water quality parameters. Four layers of material (refractive index) from the surface to the inside of the PMT are taken into account: water (1.33), glass ($1.472 + 3670/\lambda^2$, where λ is the wavelength in nm), bialkali ($n_{\rm real} + i \cdot n_{\rm img}$), and vacuum (1.0). Here, $n_{\rm real}$ and $n_{\rm img}$ are the real and imaginary parts of the complex refractive index.

Cherenkov photons are reflected or absorbed on the black sheet (Section 8.4.4). The reflectivity of the black sheet in the SK-MC is measured by a light injector set in the tank. The reflected charge was measured at three incident angles with three wavelengths.

8.5.1.3 *Energy scale calibrations in physics analyses*

The energy scale is one of the most important detector parameters. This is because the reconstructed energy is used in all physics analyses, and its uncertainty is the source of the most dominant detector systematic uncertainties in most physics analyses.

We describe how to calibrate the energy scale and estimate its uncertainty in the high-E physics analyses first. Following the various basic detector calibrations (Sections 8.5.1.1 and 8.5.1.2), the SK-MC's global photon yield is tuned using cosmic-ray through-going muon data. The Cherenkov light attenuation length used in the event reconstructions (A.1) is also determined by using cosmic-ray through-going muon MC. The electron and muon particle gun MC events are generated using the SK-MC, and the relationship between the corrected charge (A.1.2) and true momentum is obtained. The time variation of PMT gain is monitored by using the charge distribution of dark noise for each PMT. The time variation of the attenuation length is monitored by the cosmic-ray through-going muon data. Details on the attenuation length measurement analysis are available elsewhere [1]. Both time variations are taken into account in the corrected charge as a function of time.

After the above energy scale calibrations, the energy scale uncertainty is estimated using control data samples, cosmic-ray stopping muons, π^0s produced by the atmospheric neutrino interactions (Fig. 8.4), and Michel electrons from the cosmic-ray stopping muons [26, 27]. These samples are independent of the control data samples used in the prior calibrations. The uncertainty of the energy scale used in the physics analyses is estimated from the quadratic sum of the uncertainty of the absolute scale (difference between data and MC) in the calibration reference time period and the residual time variation in each SK phase. The directional dependence of the energy scale obtained using Michel electron data is also considered in the physics analyses as another energy scale error source.

For the low-E analyses, the same initial calibrations (Sections 8.5.1.1 and 8.5.1.2) are used. The energy scale is of particular importance to the solar neutrino analysis since the recoil electron spectrum from the elastic

scattering of ^{8}B solar neutrinos on electrons is steeply falling with energy. A precise calibration is performed with the LINAC (Section 8.4.2), which also checks angular resolution. To crosscheck it and to study the directional dependence of the energy scale, ^{16}N is produced via (n, p) reactions on ^{16}O using a deuterium-tritium ("DT") fusion neutron generator which makes $\sim$14 MeV neutrons [31]. ^{16}N decay is dominated by an electron whose maximum energy of 4.3 MeV coincides with gamma radiation at 6.1 MeV. Spallation from cosmic-ray muons produces neutrons that can also be used for calibration [32].

8.5.2 *OD calibration*

Requirements for OD calibration are not as stringent as for the ID in the current SK physics analyses. The readout electronics and the PMT HV power supply are similar to those for the ID (Section 8.4.6). The calibration and simulation parameter tuning for the OD-PMTs are similar but done separately from that for the ID. The PMT timing and gain calibrations are done using cosmic-ray muon and dark noise data, respectively. Cosmic-ray muon data are also used to tune the light reflection on the Tyvek® sheets (Section 8.4.4) in the SK-MC.

From the same laser used in the ID PMT timing monitor, 52 optical fibers extend through OD calibration holes (Section 8.4.2) to each OD region in the tank. A diffuser is attached to the end of each fiber. The charge nonlinearity of each readout channel is measured with all the light injector data and implemented in the SK-MC.

8.6 Future Prospects

Hyper-Kamiokande (Hyper-K or HK) [33] and KM3Net [34] are used as examples to discuss the prospects for future plans for high-E physics experiments.

8.6.1 *Densely instrumented artificial tanks*

The planned HK detector will consist of an order of magnitude larger tank than the predecessor, SK, and will be equipped with ultrahigh sensitivity photosensors. A larger HK tank will be used in order to obtain in only 10 years an amount of data corresponding to 100 years of data collection time using SK. This allows for the observation of previously unrevealed rare phenomena and to probe CP violation in

neutrino oscillation. We expect an order of magnitude higher sensitivity to nucleon decay searches. We have been developing the world's largest 50 cm PMTs, which exhibit a photodetection efficiency two times greater than that of the SK PMTs. These new PMTs are able to perform light intensity and timing measurements with a much higher precision.

Thanks to its vertical cylindrical tank which is similar to SK, there is no major concern which makes the expected energy scale error significantly larger in HK. However, it is necessary to reduce the systematic error of the energy scale in HK to reach the target physics analysis sensitivities. For this purpose, improved measurements of low-level detector parameters, such as scattering and absorption in the water and PMT performance will be pursued and linked to the uncertainties on reconstructed particle parameters. To improve physics sensitivities, a more extensive OD calibration will be performed, including the effect of water quality and Tyvek® reflectivity.

In addition to the 50 cm PMT from Hamamatsu, use of Multi-PMT ("mPMT") is currently considered in HK. The mPMT module consists of 19 PMTs of 7.5 cm diameter, contained in a vessel with a diameter of 50 cm. The mPMT module has the following advantages over the conventional 50 cm PMT:

- It has high granularity with multiple 7.5 cm PMTs, which provides higher resolution of Cherenkov ring images, especially for charged particles created at a short distance from the wall.
- Its directionality improves the reconstruction of the edge of the Cherenkov ring image, which is not recognized with 50 cm PMTs if the vertex is close to the wall. This also helps to identify the position of light emission.
- It has better timing resolution with small PMTs.

The mPMT will be also used for calibration. As the mPMT is an independent photon detection device from the 50 cm PMT system, comparing the two readout systems can investigate possible biases in one of the photo-sensor systems. Due to the large difference in the acceptance (the photo-cathode area of a 50 cm PMT is a factor 40 larger than that of the 7.5 cm PMT), the two photo-sensor systems measure different numbers of photoelectrons from the same light source. Therefore, nonlinear bias, if it exists, appears differently in 50 cm PMTs and mPMTs. The directionality and improved timing resolution of the mPMTs, combined with data from

the 50 cm PMTs, can also enable improved measurements of low-level detector parameters from calibration sources.

For large detectors, measurements necessary for calibration must be automated as much as possible. It is also necessary to find ways to further reduce detector downtime in order to not miss important physics events like supernovae.

Attempts to reconstruct events using new software techniques such as machine learning have also begun in both SK and HK. These new techniques are expected to improve the performance of event reconstruction.

8.6.2 *Sparsely instrumented natural water*

The Cubic Kilometer Neutrino Telescope, or KM3NeT, is a future European research infrastructure that will be located at the bottom of the Mediterranean Sea. It will host the next-generation neutrino telescope in the form of a water Cherenkov detector with an instrumented volume of several cubic kilometers distributed over three locations in the Mediterranean.

KM3NeT will search for neutrinos from distant astrophysical sources like Core-Collapse Supernovae (CCSN), the dramatic explosions of giant stars at the end of their evolution, or their remnants (SNR), gamma-ray bursts, or colliding stars and will be a powerful tool in the search for dark matter in the universe. Its prime objective is to detect neutrinos from sources in our galaxy. Arrays of thousands of optical sensor modules will detect the faint light in the deep sea from charged particles originating from collisions of the neutrinos and the water or rock in the vicinity of the detector.

The KM3NeT telescope will consist of two sites, realizing two neutrino telescopes: ARCA and ORCA. With the ARCA telescope, which is more sparsely instrumented but has a larger volume, KM3NeT will be sensitive to higher-energy, lower-rate distant astrophysical sources, such as gamma-ray bursts or colliding stars. The ORCA telescope is more densely instrumented and will be sensitive to lower energy neutrinos, and is the instrument for KM3NeT scientists studying neutrino properties by exploiting neutrinos generated in the Earth's atmosphere.

ARCA will be installed at the KM3NeT-It site, about 100 km offshore of the small town of Portopalo di Capo Passero in Sicily, Italy. The detection units of the ARCA telescope will be anchored at a depth of about 3,500 m. With an appropriate granularity of the three-dimensional arrays of sensor modules in the detector of the ARCA telescope, cosmic neutrinos with energies between several tens of GeV and 100 PeV can be observed [35].

Deployed at the KM3NeT-Fr installation site about 40 km offshore from Toulon, France, the ORCA neutrino detector will take advantage of the excellent optical properties of deep-sea water to achieve the angular and energy resolutions required for resolving the neutrino mass hierarchy. A multi-megaton scale array of KM3NeT light sensor modules will be used with a granularity optimized for studying reactions of atmospheric neutrinos with the seawater. The sensor modules will be arranged on vertical detection units with a height of about 150 m and in the dense configuration required for detection of neutrinos with energies as low as about a GeV, three orders of magnitude lower than the typical energy scale probed by the detector of the ARCA telescope for neutrino astroparticle physics.

In the future and pending funding, the full neutrino telescope will contain on the order of 12,000 pressure-resistant glass spheres attached to about 600 strings. The strings hold sensor spheres, each anchored to the sea floor and supported by floats. Each sphere, called a "digital optical module" (DOM), is about 43 cm in diameter, contains 7.6 cm PMTs with supporting electronics, and is connected to shore via a high-bandwidth optical network. At the shore of each KM3NeT installation site, a farm of computers will perform the first data filter in the search for the signal of cosmic neutrinos, prior to streaming the data to a central KM3NeT data center for storage and further analysis.

8.6.3 *Contrasts and complementarities with DUNE*

A future detector with overlapping physics aims with respect to next-generation water Cherenkov detectors is the Deep Underground Neutrino Experiment (DUNE). DUNE is a 40-kton liquid argon time-projection chamber (LArTPC) planned for an underground site in South Dakota, in conjunction with a neutrino beam from Fermilab. LArTPC technology has advantages and disadvantages with respect to water Cherenkov technology; in particular, LArTPCs provide fine-grained tracking capability without a Cherenkov threshold so that hadronic components of final-state products of neutrino interactions are not lost. The disadvantage of LArTPCs is greater cost and complexity; water detectors can be made very large for a relatively low cost per kiloton and so often win in statistics. There are many complementarities between the detector types, depending on the physics topic. An especially notable complementarity is that for supernova neutrinos; water is primarily sensitive to electron antineutrinos via inverse beta decay on free protons, whereas LAr is primarily sensitive to electron

neutrinos via charged-current absorption on ^{40}Ar. Having both types of detectors active during the next supernova burst will greatly enhance the worldwide scientific reach.

8.7 Achievement of Cherenkov Neutrino Detectors

Large water Cherenkov detectors have accumulated many very high-impact scientific achievements over the past decades. The first-generation Kamiokande-II experiment made the first directional solar neutrino measurement; Kamiokande-II and IMB were the first to observe hints of atmospheric neutrino disappearance. Both Kamiokande-II and IMB made the historic observation of a neutrino burst from SN 1987A in the Large Magellanic Cloud. "For pioneering contributions to astrophysics, in particular for the detection of cosmic neutrinos," Masatoshi Koshiba was awarded the Nobel Prize in Physics in 2002 [36]. The next generation of water Cherenkov detectors brought precision solar-neutrino oscillation information by Super-K and SNO, along with clear evidence of atmospheric neutrino oscillation by Super-K. These measurements resulted in the Nobel Prize to Takaaki Kajita and Arthur B. McDonald in 2015 [37]. Furthermore, Super-K was and is the far detector for the K2K and T2K long-baseline experiments, which confirmed atmospheric neutrino oscillations with artificial neutrino beams and improved knowledge of oscillation parameters. In addition, IceCube has made the first observations of cosmic neutrinos, both as a diffuse flux and from specific sources. Super-K has also produced stringent limits on baryon number violation via many channels — while baryon number violation has not been observed, this lack of observation has been highly influential for constraining grand unified theories. These achievements represent only a few highlights. Super-K, SNO, and long-string neutrino telescopes have produced decades of additional science, including indirect dark matter constraints, cosmic ray measurements, astrophysical neutrino source searches, and diverse searches for beyond-the-standard-model physics.

Appendix A: Event Reconstruction Algorithm in SK

This appendix describes the reconstructions of "fully contained" events (Section 8.4.11) in the current SK physics analyses. For comparison with high-E physics event reconstruction, low-E physics event reconstruction is also described. Some future prospects are mentioned in Section 8.6.1.

A.1 High-E Physics Analyses

In the high-E neutrino interactions ($>\sim$100 MeV), we reconstruct the physics quantities of an event, such as vertex position, the number of Cherenkov rings, momentum, particle type, and the number of Michel electrons. The primary event fitter is called "APfit" [38]. We start from the vertex fitter program to obtain the vertex position of events. With the knowledge of the reconstructed vertex, the ring fitter identifies each ring. After that, the particle identification program identifies the particle type for each ring. The momentum for each ring is determined and Michel electrons are identified.

A.1.1 *Vertex*

The principle of the vertex fitting is that the timing residual (i.e., (photon arrival time) − (time of flight)) distribution should be most peaked with the correct vertex position. In the timing distribution, the time resolution of each hit PMT as a function of detected photoelectrons (Section 8.5.1.1) and the track length of the charged particle (Section 8.2.2) are taken into account.

The timing fit has worse vertex resolution in the direction of Cherenkov ring, compared to that in the perpendicular direction. This is because the time residual does not change along the line on which the distance from all hit PMTs is the same. For single-ring events, the Cherenkov ring charge pattern information in addition to the timing information is used to improve the vertex reconstruction in the longitudinal direction. The expected and observed photoelectrons are compared for each hit PMT to optimize the reconstructed vertex. The result of the particle identification (A.1.4) is used in the expectation.

A.1.2 *Ring fitting*

Possible Cherenkov rings are looked for and probable rings are reconstructed in the ring fitter. We use a known technique for pattern recognition, the Hough transformation [39], to search for possible ring candidates. The Hough transformation transforms rings of an assumed radius to peaks in Hough space (see Fig. 8.12). In the ring fitter, the Hough space is made up of two-dimensional arrays divided by polar angle Θ and azimuthal angle Φ. These angles are measured from the reconstructed vertex. Detected photoelectrons in each hit PMT are mapped to the (Θ, Φ)

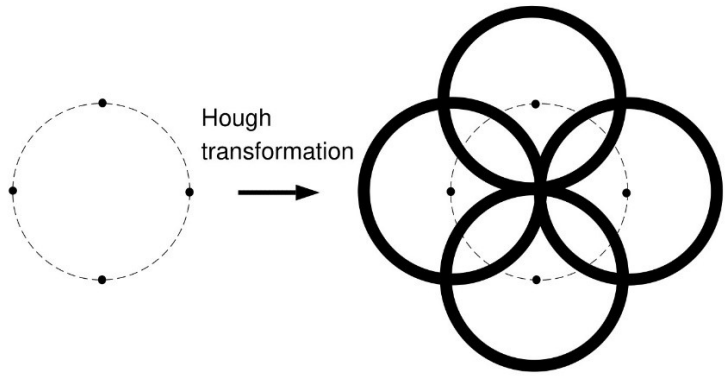

Figure 8.12. Principle of the ring fitting [38] Suppose there are four hit PMTs on the unknown ring (radius r) and we want to find the center of the ring (left figure). By Hough transformation, the detected photoelectrons are mapped to a circle with radius r centered on the PMT (right figure). By accumulating the mapped circles, we can find the peak in the Hough space, giving the center of the unknown ring.

pixels. The number of photoelectrons is corrected ("corrected charge") by taking into account the distance from the vertex, the attenuation length of Cherenkov light in water, time variation of the PMT gain (Section 8.5.1.3), and acceptance of the PMT as a function of photon incident angle. Then, we draw a circle of a fixed radius R corresponding to a 42° Cherenkov cone from each hit PMT. By accumulating the mapped circles, we can find the peak in the Hough space, giving the center of the unknown ring.

If the momentum of one of the reconstructed rings is too low, or if the direction of the ring is too close to the other, this ring is discarded as a fake ring by the ring correction program for the multi-ring candidate events. This is to avoid double counting of the number of rings due to an additional Cherenkov ring from scattering of a single charged particle, for example.

A.1.3 *Ring edge finding*

The Cherenkov opening angle (Eq. (8.1)) is reconstructed for each ring by using the photoelectron distribution as a function of the opening angle, as shown in Fig. 8.13. As shown in the lower plot, the edge of the ring is reconstructed at the second derivative = 0 above the peak angle in the upper plot.

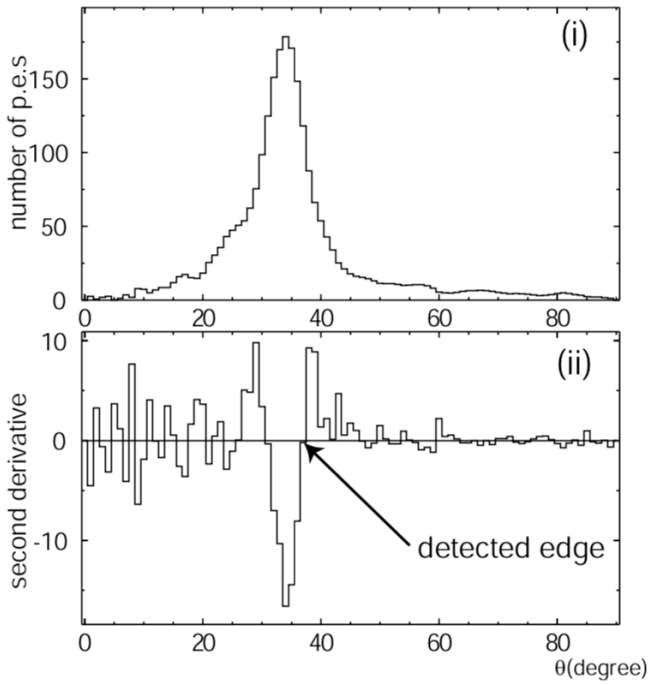

Figure 8.13. Typical observed photoelectrons as a function of the opening angle in the upper plot [38]. The second derivative from the upper distribution in the lower plot.

A.1.4 *Particle identification*

The primary particle identification (PID) classifies a particle as a showering particle ($e^{\pm}$, γ) or a non-showering particle ($\mu^{\pm}$, $\pi^{\pm}$, etc.), using the photon distribution of its Cherenkov ring (Fig. 8.3, for example). Showering (non-showering) particles are called "electron-like" ("muon-like"). At first, the expected photoelectron distributions are calculated with an assumption of the particle type. Using the expected photoelectron distributions, the likelihood is calculated for the electron and muon assumptions, respectively. The calculation of the probability is performed for all of the PMTs for which the opening angles toward the ring direction are within 1.5 times the Cherenkov opening angle. The particle type (electron-like or muon-like) with greater likelihood is chosen. Optimizations of the expected charges are performed by changing the direction and the Cherenkov opening angle of the ring, in order to get maximum-likelihood values.

Additionally, another probability is defined using only the Cherenkov opening angle to utilize the β dependence (Eq. (8.1)). The Cherenkov angle of muons with lower momentum ($<\sim$500 MeV/c) is smaller than 41°. Depending on the needs of the physics analysis, the second likelihood can be combined with the first one, or not. For example, the selection of the π^0 events (Fig. 8.4) does not use the second likelihood. This is because the gamma radiation length in water is $\sim$36 cm (no Cherenkov light emission), and the event vertex is reconstructed at the electron–positron pair-production point instead of the π^0 decay point.

The excellent PID performance (e/π^0 separation) was experimentally confirmed using a 1-kiloton water Cherenkov detector with electron and muon beams from the 12 GeV proton synchrotron at KEK [40].

Some physics analyses use recoil protons (a mass of 938 MeV/c^2) with energies above the Cherenkov threshold (1.4 GeV) [41, 42]. Muons and protons both have sharp ring edges, whereas electrons produce fuzzy rings and are relatively easy to distinguish. To distinguish protons from muons, a proton fitter using the light pattern and ring topology has been developed (see Ref. [41] for details). A characteristic of protons is that they tend to have hadronic interactions in water and lose energy by producing secondary particles. If both the secondary particles and the scattered proton are below the Cherenkov threshold, the Cherenkov light emission is truncated and leaves a narrow proton Cherenkov ring, for example.

A.1.5 *Ring separation*

The ring separation program determines the fraction of photoelectrons in each PMT for each ring for multi-ring events. We need this separation for the ring fitting and the particle identification of each ring as well as the momentum reconstruction.

Given a vertex position and each ring direction, the expected photoelectron distribution for each ring as a function of opening angle is calculated assuming the flat distribution in azimuthal angle. The PID result is used to calculate the expected charge. The charge fraction for each ring is determined by comparing the expected and observed charges for different fractions.

A.1.6 *Momentum*

The momentum is estimated from the total sum of the corrected charge within a 70° half opening angle from the reconstructed ring direction. To

reconstruct momentum from the corrected charge, conversion tables are prepared based on the electron and muon particle gun MC events. The PID results define electron-like or muon-like momentum, respectively. For multi-ring events, the ring separation program is applied with each particle-type assumption to determine the fraction of photoelectrons in each PMT due to each ring. Then, the momentum for each ring is determined by the same method used for single-ring events.

The energy (momentum) scale calibrations and checks dedicated for each physics analysis using several control data samples are described in Section 8.5.1.3.

A.1.7 *Michel electron tagging*

We identify Michel electrons, namely, the electrons produced when muons decay, following the primary events. Michel electron candidates are detected when the number of hits in the sliding timing window of a few 10 ns after the primary event exceeds a certain threshold, the vertex is well reconstructed, and the total number of photoelectrons does not exceed a certain threshold.

A.1.8 *Alternative fitter*

Depending on the physics analyses, the other fitter called "fiTQun" can be applied [13, 43, 44]. FiTQun employs a maximum likelihood method to reconstruct particle types and determine kinematics in the detector simultaneously. The algorithm is based on methods developed for the MiniBooNE experiment [45] but has been developed from scratch for SK with additional features, such as multi-ring reconstruction for events with multiple final-state particles. Compared to APFit, fiTQun uses more information, including information from PMT hits outside of the expected Cherenkov cone and hit timing information, during the fitting procedure. For a given event, fiTQun's fit procedure will run multiple times to determine the best kinematic parameters for each possible particle configuration hypothesis, while APFit basically fits those parameters once. Since fiTQun uses more information, the fitting process time is slower and a better understanding of the detector parameters implemented in the detector simulator (Section 8.5.1) is required with respect to APfit.

Unlike APfit, a charged pion hypothesis with a single track compatible with a charged pion undergoing a hard scatter can be used [46].

A.2 Low-E Physics Analyses

There are several differences in the reconstruction of "low-E" neutrino interactions ($\ll$100 MeV): particle identification is less important since almost all resulting charged particles are electrons and gamma rays, and remaining muons or pions are barely above the Cherenkov threshold, so the ring opening angle is significantly smaller than 41°. Also, events with multiple rings typically cannot be separated, so the ring fitter is replaced by cuts designed to suppress multi-ring events. Due to multiple Coulomb scattering of electrons due to neutrino interactions or Compton scattering of gamma rays, ring patterns are less clear than those resulting from high-E interactions. Also, individual PMTs typically record only single-photoelectrons. As a consequence, vertex reconstruction is based almost exclusively on PMT timing. Recorded pulse heights only reflect the single-photoelectron distribution, and the PMT hit pattern does not help much.

The "BONSAI" (Branch Optimization Navigating Successive Annealing Iterations) event reconstruction [47] compares the hit time residual distribution (assuming direct photon travel from that point to the PMT) viewed from a single point in space-time (the 3D vertex combined with the assumed time of light emission) with a likelihood. The point with the largest likelihood is chosen as the reconstructed vertex. To find the maximum, BONSAI uses a simple search tree, combined with an annealing algorithm designed to avoid local maxima: instead of selecting a single, best branch to continue, all branches within a range of likelihoods are continued. This is particularly important for the lowest electron energies since dark noise fluctuations combined with radioactive background from the detector boundaries can result in several local maxima deep inside the detector. The tree is started from multiple points calculated from sets of "four-hit combinations." A four-hit combination results in an analytical exact solution to the four equations corresponding to the four-hit times. The four-hit combinations are drawn from a subset of PMT hits. That subset is constructed from the requirement that every hit pair has a time difference smaller than their spatial separation, divided by the speed of light in water.

Once a vertex is determined, another likelihood fit determines the event direction after hits are selected within 20 ns in the time-of-flight subtracted hit times. This likelihood is energy dependent. At first, an initial energy estimate is used; after the full energy reconstruction is finished, the direction likelihood fit is repeated.

In addition to the direction reconstruction, three-hit combinations are formed from the 20 ns hit selection and the Cherenkov angle distribution is made from these (each three-hit combination gives an exact solution of the opening angle). Multiple photon events result in a peak of this distribution that is larger than 41°, while muons and pions have a peak below this angle. Electrons always have velocities close to the speed of light if they emit Cherenkov light at all, so their opening angle is always near 41°. The amount of multiple Coulomb scattering is estimated from the "sharpness" of the Cherenkov cone by forming event direction candidates from hit pairs and comparing the length of the vector sum of these candidates to the maximal possible length (number of such pairs). Electrons undergoing a larger than usual amount of multiple Coulomb scattering are typically lower in energy and are observed only due to an up-fluctuation in light yield. An example is ^{210}Bi beta decay (with an endpoint energy of $\sim$3 MeV). Also, beta-gamma decays such as ^{208}Tl (endpoint $\sim$5 MeV) look like single-photoelectrons with a larger than usual amount of multiple Coulomb scattering.

The energy is reconstructed by counting PMT hits within 50 ns after time-of-flight subtraction. Multiple photon hits are corrected by PMT occupancy. Additional corrections are made to account for water transparency, late arrival photons, dark noise, number of dead PMTs, effective cathode area of the PMT, and PMT gain variation.

Neutrons may be generated by neutrino interactions. To detect the neutron signal, two independent approaches have been implemented. The first approach is to detect the single 2.2 MeV gamma released from neutron capture on hydrogen. This approach requires a 500-μs forced trigger scheme following a normal trigger, in order to identify the 2.2 MeV gamma offline [48]. The second approach involves doping the water with a water-soluble chemical compound of gadolinium (Section 8.4.9), neutron capture on which yields a gamma cascade with a total energy of about 8 MeV. These relatively high-energy gamma rays should be readily seen in SK-VI [3], SK-VII [4], and SK-VIII.

Acknowledgments

The author would like to thank the following people (in alphabetical order): Hans-Gerd Berns, Yoshinari Hayato, Edward Kearns, Yusuke Koshio, Fabio Lacob, Shigenobu Matsuno, Neil Kevin McCauley, Makoto Miura, Masayuki Nakahata, Yuichi Oyama, Gianfranca de Rosa, Seiya Sakai, Kate

Scholberg, Hiroyuki Sekiya, Masato Shiozawa, Michael Smy, Henry W. Sobel, Yasuo Takeuchi, and Roger A. Wendell.

References

[1] Y. Fukuda *et al.* The super-Kamiokande detector. Nuclear Instruments and Methods in Physics Research Section A: Accelerators, Spectrometers, Detectors and Associated Equipment, 501:418–462, 2003.

[2] K. Abe *et al.* Calibration of the super-Kamiokande detector. Nuclear Instruments and Methods in Physics Research Section A: Accelerators, Spectrometers, Detectors and Associated Equipment, 737:253–272, 2014.

[3] K. Abe *et al.* First gadolinium loading to Super-Kamiokande. Nuclear Instruments and Methods in Physics Research Section A: Accelerators, Spectrometers, Detectors and Associated Equipment, 1027:166248, 2022.

[4] K. Abe *et al.* Second gadolinium loading to Super-Kamiokande, *Nuclear Instruments and Methods in Physics Research A* 1065 (2024) 169480.

[5] R. M. Bionta *et al.* Observation of a neutrino burst in coincidence with supernova 1987a in the large Magellanic cloud. *Physical Review Letters*, 58:1494, 1987.

[6] K. Hirata *et al.* Observation of a neutrino burst from the supernova SN1987A. *Physical Review Letters*, 58:1490, 1987.

[7] L. A. Cole. *Chasing the Ghost, Nobelist Fred Reines and the Neutrino*. Rutgers University, USA, March 2021. https://doi.org/10.1142/12125, https://www.worldscientific.com/worldscibooks/10.1142/12125.

[8] J. D. Jackson. *Classical Electrodynamics,* 3rd edn. Wiley, New York, 1999, pp. 637–638.

[9] K. Abe *et al.* Search for nucleon decay into charged antilepton plus meson in 0.316 megaton · years exposure of the super-Kamiokande water Cherenkov detector. *Physical Review D*, 96:012003, 2017.

[10] Z. Li *et al.* Measurement of the tau neutrino cross section in atmospheric neutrino oscillations with super-Kamiokande. *Physical Review D*, 98:052006, 2018.

[11] Y. Fukuda *et al.* Evidence for oscillation of atmospheric neutrinos. *Physical Review Letters*, 81:1562, 1998.

[12] M. H. Ahn *et al.* Measurement of neutrino oscillation by the K2K experiment. *Physical Review D*, 74:072003, 2006.

[13] K. Abe *et al.* Improved constraints on neutrino mixing from the T2K experiment with 3.13×10^{21} protons on target. *Physical Review D*, 103:112008, 2021.

[14] S. Nakayama *et al.* Measurement of single π^0 production in neutral current neutrino interactions with water by a 1.3 GeV wide band muon neutrino beam. *Physics Letters B* 619:255–262, 2005.

[15] S. Mine *et al.* Experimental study of the atmospheric neutrino backgrounds for $p \rightarrow e^+\pi^0$ searches in water Cherenkov detectors. *Physical Review D,* 77:032003, 2008.

[16] K. K. Young *et al.* DUMAND-II (deep underwater muon and neutrino detector) progress report. *AIP Conference Proceedings*, 338:886, 1995.

[17] I. A. Belolaptikov *et al.* The Baikal underwater neutrino telescope: Design, performance, and first results. *Astroparticle Physics*, 7:263–282, 1997.

[18] S. Adrián-Martínez *et al.* Measurement of atmospheric neutrino oscillations with the ANTARES neutrino telescope. *Physics Letters B*, 714:224–230, 2012.

[19] J. Ahrens *et al.* Observation of high energy atmospheric with the Antarctic muon and neutrino detector array. *Physical Review D*, 66:012005, 2002.

[20] M. G. Aartsen *et al.* Evidence for high-energy extraterrestrial neutrinos at the IceCube detector. *Science*, 342, 2013.

[21] J. Boger *et al.* The Sudbury neutrino observatory. Nuclear Instruments and Methods in Physics Research Section A: Accelerators, Spectrometers, Detectors and Associated Equipment, 449:172–207, 2000.

[22] Q. R. Ahmad *et al.* Direct evidence for neutrino flavor transformation from neutral-current interactions in the Sudbury neutrino observatory. *Physical Review Letters*, 89:011301, 2002.

[23] S. N. Ahmed *et al.* Measurement of the total active ^{8}B solar neutrino flux at the Sudbury neutrino observatory with enhanced neutral current sensitivity. *Physical Review Letters*, 92:181301, 2004.

[24] B. Aharmim *et al.* Independent measurement of the total active ^{8}B solar neutrino flux using an array of ^{3}He proportional counters at the Sudbury neutrino observatory. *Physical Review Letters*, 101:111301, 2008.

[25] M. Nakahata *et al.* Calibration of super-Kamiokande using an electron LINAC. Nuclear Instruments and Methods in Physics Research Section A: Accelerators, Spectrometers, Detectors and Associated Equipment, 421:113–129, 1999.

[26] K. Abe *et al.* Atmospheric neutrino oscillation analysis with external constraints in super-Kamiokande I-IV. *Physical Review D*, 97:072001, 2018.

[27] A. Takenaka *et al.* Search for proton decay via $p \to e + \pi^0$ and $p \to \mu + \pi^0$ with an enlarged fiducial volume in super-Kamiokande I-IV. *Physical Review D*, 102:112011, 2020.

[28] H. Nishino *et al.* High-speed charge-to-time converter ASIC for the super-Kamiokande detector. Nuclear Instruments and Methods in Physics Research Section A: Accelerators, Spectrometers, Detectors and Associated Equipment, 610:710–717, 2009.

[29] H. G. Berns *et al.* GPS time synchronization system for K2K. In: *11th IEEE NPSS*, 1999, p. 480.

[30] Y. Nakano *et al.* Measurement of radon concentration in super-Kamiokande's buffer gas. Nuclear Instruments and Methods in Physics Research Section A: Accelerators, Spectrometers, Detectors and Associated Equipment, 867:108–114, 2017.

[31] E. Blaufuss *et al.* ^{16}N as a calibration source for super-Kamiokande. Nuclear Instruments and Methods in Physics Research Section A: Accelerators, Spectrometers, Detectors and Associated Equipment, 458:638–649, 2001.

[32] S. Locke *et al.* New methods and simulations for cosmogenic induced spallation removal in super-Kamiokande-IV. arXiv:2112.00092.
[33] K. Abe *et al.* Hyper-Kamiokande design report. arXiv: 2101.05269.
[34] S. Adrián-Martínez *et al.* Letter of intent for KM3NeT 2.0. arXiv: 1601.07459.
[35] F. Benfenati *et al.* First scientific results of the KM3NeT neutrino telescope. *EPJ Web of Conferences*, 283:04009, 2023.
[36] The Nobel Prize in Physics 2002. https://www.nobelprize.org/prizes/physics/2002/summary/.
[37] The Nobel Prize in Physics 2015. https://www.nobelprize.org/prizes/physics/2015/summary/.
[38] M. Shiozawa, Reconstruction algorithms in the super-Kamiokande large water Cherenkov detector. *Nuclear Instruments and Methods in Physics Research Section A: Accelerators, Spectrometers, Detectors and Associated Equipment*, 433:240–246, 1999.
[39] E. R. Davies. *Machine Vision: Theory, Algorithms, Practicalities*. Academic Press, San Diego, 1997.
[40] S. Kasuga *et al.* A study on the e/μ identification capability of a water Cerenkov detector and the atmospheric neutrino problem. *Physics Letters B*, 374:238–242, 1996.
[41] M. Fechner *et al.* Kinematic reconstruction of atmospheric neutrino events in a large water Cherenkov detector with proton identification. *Physical Review D*, 79:112010, 2009.
[42] K. Abe *et al.* Search for cosmic-ray boosted sub-GeV dark matter using recoil protons at super-Kamiokande. *Physical Review Letters*, 130:031802, 2023.
[43] K. Abe *et al.* Evidence of electron neutrino appearance in a muon neutrino beam. *Physical Review D*, 88:032002, 2013.
[44] M. Jiang *et al.* Atmospheric neutrino oscillation analysis with improved event reconstruction in super-Kamiokande IV. *Progress of Theoretical and Experimental Physics*, 053F01, 2019, 39 p.
[45] R. B. Patterson *et al.* The extended-track event reconstruction for MiniBooNE. Nuclear Instruments and Methods in Physics Research Section A: Accelerators, Spectrometers, Detectors and Associated Equipment, 608:206, 2009.
[46] N. F. Calabria. Search for proton decay in super-Kamiokande and perspectives in the hyper-Kamiokande experiments. PhD Thesis, The University of Naples Federico II, 2022.
[47] K. Abe *et al.* Solar neutrino measurements in super-Kamiokande-IV. *Physical Review D*, 94:052010, 2016.
[48] H. Watanabe *et al.* First study of neutron tagging with a water Cherenkov detector. *Astroparticle Physics*, 31:320–328, 2009.